# Sensitivity of DynaWhirlpool hydrocyclone operation to applied back-pressure

M. Piller [a,*], G. Schena [a], G. Belardi [b]

[a] Department of Engineering and Architecture, Università degli Studi di Trieste, via A. Valerio, 10-34127 Trieste (TS), Italy
[b] Istituto di Geologia Ambientale e Geoingegneria, Consiglio Nazionale delle Ricerche, 00015 Monterotondo (RM), Italy

ARTICLE INFO

Accepted 28 July 2016

*Keywords:*
DynaWhirlpool
Cylindrical hydrocyclone
Two-phase flow
Sensitivity analysis
Back-pressure
CFD

ABSTRACT

The two-phase, air–water flow pattern in a DynaWhirlpool centrifugal separator is investigated using time-dependent, three-dimensional numerical simulation. The air–water interface is captured by the Volume-Of-Fluid approach, while the unresolved turbulence fluctuations are modeled via a second-order differential-stress turbulence model. Among the different operating variables, the back-pressure at the sink outlet affects significantly the flow within the cyclone. The modifications experienced by the flow field as the back-pressure is increased are documented and interpreted. The variation of relevant operating variables is also reported, as the split ratio and the Euler number characterizing the device. It is verified that for large values of the back-pressure the water flow through the sink is hindered and the air core disappears. The flow pattern is moderately altered when the cyclone is fed with a non-Newtonian fluid with the same viscosity as a real water/magnetite dense medium.

## 1. Introduction

Cylindrical hydrocyclones are centrifugal separators mainly used to separate solid materials by density. This work deals with the DynaWhirlpool cylindrical hydrocyclone (DWP henceforth) (Rakowsky, 1959). In a DWP cylindrical hydrocyclone the dry, raw material is fed axially by gravity through an upper *feed* pipe (FEP hereafter) rather than pumped as in traditional hydrocyclones, after having been pre-screened to eliminate the fine sizes, e.g. $<0.5 \div 1.0$ mm. A modest amount of circulating medium (or *dense* medium), no more than 10% by weight, is pre-mixed with the raw material to improve the mixture's fluidity. The dense medium is pumped into the separator through a tangential or involute *medium inlet* port (MIP henceforth) at the bottom of the cylindrical body (the *barrel*). Under *usual* operating conditions, an ascending helicoidal flow develops near the barrel's wall (Wills, 1988; Piller et al., in press), where the fluid moves upwards close to the wall and part of it is discharged tangentially through the top *sink* port (SIP henceforward), conveying the heavier particles migrated towards the outer wall by the combined action of the centrifugal and buoyancy forces. The remaining fluid, carrying the lighter particles, overturns and spirals downwards towards the *float* outlet (FLP hereinafter) where it can either be discharged axially or can experience another flow reversal. This flow pattern allows to categorize the DWP as a *reverse-*, *swirling-flow* separator. Air enters the barrel through both axial openings and forms a stable air core flowing downwards. The device is often operated 15 to 30° tilted with respect to the horizontal.

A number of single- and multi-stage cylindrical separators are closely derived from the DWP (e.g., Ruff (1980)). The TriFlo™ centrifugal separator (Ferrara and Ruff, 1982; Ferrara, 1995) consists of two identical DWP stages arranged in series (Chiné and Ferrara, 1997). The float product of the first TriFlo™ stage feeds the second stage. The Large Coal Dense Medium Separator (LARCODEM) adopts the same DWP geometry with the addition of a vortex extractor at the sink outlet. A three-product LARCODEM has been built and tested extensively in coal cleaning (Baillie et al., 1997). Miller and Van Camp (1982) propose an *air-sparged* cylindrical hydrocyclone for fine-coal floatation. Chiné and Concha (2000) carry out an experimental campaign of laser Doppler measurements of tangential and axial velocities on a 100 mm transparent laboratory TriFlo™. Belardi et al. (2014) use these experimental data to set up and tune a CFD model of the TriFlo™ considered by Chiné and Concha (2000). The first stage of this model is used by Piller et al. (in press) to investigate the two-phase, air–water flow within a DWP hydrocyclone.

In the present work the CFD model of Piller et al. (in press) is used to carry out a sensitivity analysis with respect to the back pressure applied at the sink port (henceforth referred to as BPS). The BPS is commonly set by rising adjustable discharge pipes. A range of BPS values, allowing for the development of a stable air core, is explored. In a DWP, air enters through the feed port and leaves from the float port. In this study, water is injected through the medium inlet port and leaves the device

* Corresponding author.
*E-mail addresses:* piller@units.it (M. Piller), schena@units.it (G. Schena), girolamo.belardi@igag.cnr.it (G. Belardi).

through the sink port. It is verified that, for excessively high values of BPS water enters the device through the sink port, a stable air core is not formed and water leaves the device through both the feed and the float ports. The back-pressure strongly affects both the air core shape and stability while it is verified that the position and size of the zero axial velocity mantle are roughly independent of the BPS.

A numerical simulation is carried out, in order to access the impact of the dense medium density and viscosity on the resulting flow pattern. A non-Newtonian, single-phase fluid, with the same density of a water/magnetite dense medium (relative density 1.6) is injected through the MIP in place of water. The rheological model proposed by Lapasin et al. (1988) is used to relate viscosity and shear rate. The relative dynamic viscosity, determined by the simulated shear rate, ranges from 2.5 to 3.3. The resulting tangential and axial velocity components are weakly damped with respect to the case where water is injected through the MIP, while the radial velocity component is sensibly impaired.

## 2. Materials and methods

Two opposite views of the considered cyclone geometry are represented in Fig. 1. The device consists of a cylindrical barrel of height $H_c$ and internal diameter $D_c$, a *feed* pipe of inner diameter $d_f$, penetrating into the barrel for a depth $h_f$, a *float* pipe of inner diameter $d_{fl}$, penetrating into the barrel for a depth $h_{fl}$, an inlet involute (*medium inlet*) with square inlet cross-section of side $a_i$, located in the lower part of the barrel, an outlet involute (*sink outlet*) with square outlet cross-section of side $a_o$, located in the upper part of the barrel. The values of the geometrical parameters used in the present study are reported in Table 1. The cyclone is 25° tilted with respect to the horizontal.

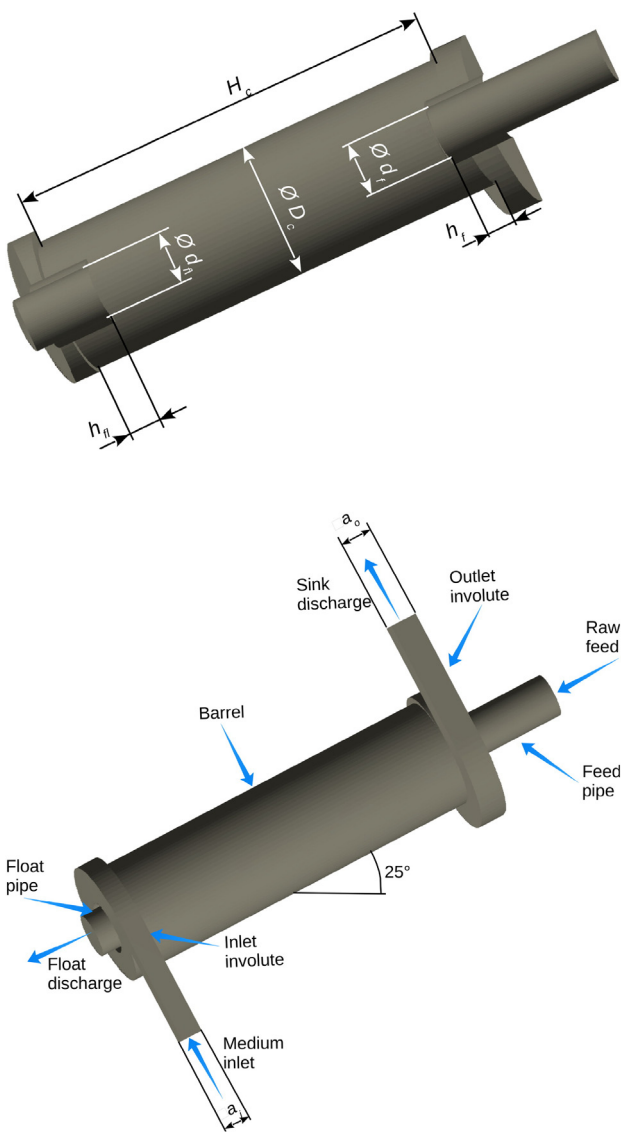


**Fig. 1.** Two opposite views of the considered hydrocyclone.

Water is injected through the *medium inlet* port with a mean velocity of 2.86 m/s, corresponding to a Reynolds number (based on hydraulic diameter) of $5.7\times10^4$. The Reynolds number based on cyclone's diameter is $2.8\times10^5$. The device is open to the atmosphere through the *feed* and *float* ports, while a counter-pressure is applied to the *sink port*. The aforementioned boundaries are represented by the following mathematical models: velocity inlet for the MIP, pressure outlet with static pressure $p=0$ Pa for both the FEP and FLP, pressure outlet with $p=$ *BPS* Pa for the SIP. As the present study focuses on the fundamental hydraulic behavior of the DWP, plain water is injected through the MIP. Water and air are considered as Newtonian, immiscible fluids with constant density, viscosity and surface tension coefficient. Compressibility effects, solubility of air in water and solid-surface wettability are neglected. In addition, the flow is assumed to be isothermal.

The time-dependent, Reynolds-Averaged Navier–Stokes equations for a two-phase mixture are solved numerically by the finite volume commercial package ANSYS FLUENT™ version 16.1. Details on the relevant governing equations and numerical approach are provided in (Piller et al., in press), where the proposed model is validated by comparing simulated results against experimental data. A high-quality, block-structured computational mesh consisting of 153,918 hexahedral cells is built with the ANSYS ICEM™ commercial package. The time-step used to advance all simulations is $\Delta t=0.0001$ s, yielding maximum and volume-averaged values of the Courant–Friedrichs–Lewy number of approximately 5 and 0.1, respectively, for the case with BPS = 3035 Pa. The simulation with BPS = 3035 Pa required about two *flow-through* times (i.e., twice the time required to fill the volume of the cyclone by the assigned inlet volume flow rate) to reach a statistically-steady state, i.e., approximately 6 s. The simulations corresponding to different values of BPS were initiated from a *converged* state of a previous simulation with a close value of *BPS*, then allowed to *relax* for about 1 flow-through time before collecting any data.

Various turbulence models have been used over the years to simulate the flow field within hydrocyclones. Recent studies (Slack and Wraith, 1997; Slack et al., 2000; Suasnabar, 2000; Cullivan et al., 2003) suggest that the flow within hydrocyclones is far too anisotropic to be simulated accurately by two-equation models, which inherently neglect the energy-redistribution mechanism of the pressure-rate-of-strain tensor (Pope, 2000). A three-dimensional, two-phase flow simulation of a 350 mm Dutch State Mines pattern body using a differential Reynolds stress model (Brennan et al., 2002) predicts the position of the air core and the flow splits with reasonable accuracy. Brennan (2006) carries out three-dimensional, two-phase flow (water/air) simulations of the 75 mm hydrocyclone already considered by Hsieh and Rajamani (1991). Turbulence is resolved by the Smagorinsky–Lilly subgrid scale model (Smagorinsky, 1963; Lilly, 1966) or by the differential Reynolds stress turbulence model (Launder et al., 1975). According to Brennan (Brennan, 2006), Large Eddy Simulation results are in remarkable agreement with experimental data provided a sufficiently fine mesh is used, while the Reynolds stress model underpredicts the tangential velocities, with little difference between the linear (Launder, 1989) and the quadratic (Speziale et al., 1991) pressure-rate-of-strain models (LPS and QPS, respectively). The QPS model (Speziale et al., 1991) is adopted in Piller et al. (in press), where a single

**Table 1**
Values of the geometrical parameters (in millimetres) for the considered device.

| $H_c$ | $D_c$ | $d_f$ | $h_f$ | $d_{fl}$ | $h_{fl}$ | $a_i$ | $a_o$ |
|---|---|---|---|---|---|---|---|
| 320 | 100 | 40 | 25 | 40 | 22 | 20 | 20 |

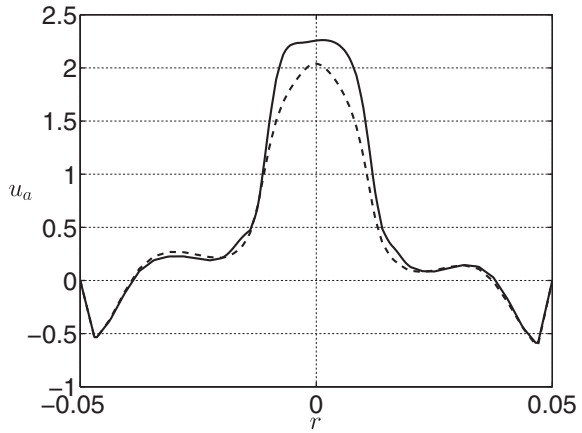


**Fig. 2.** Comparison of axial velocity $u_a$ in m/s for the case BPS = 3035 Pa, with either LPS (dashed line) or QPS (solid line) Pressure-Rate-of-Strain models.

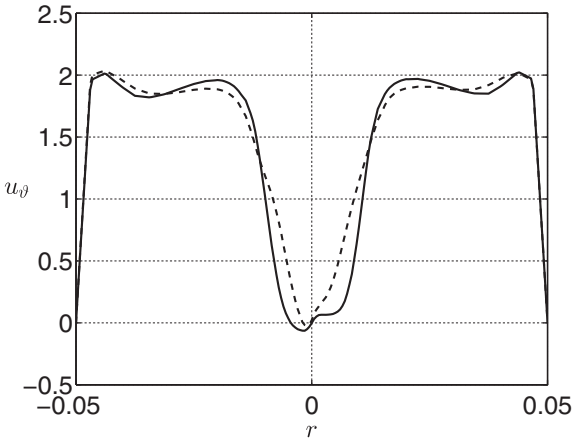


**Fig. 4.** Comparison of tangential velocity $u_\theta$ in m/s for the case BPS = 3035 Pa, with either LPS (dashed line) or QPS (solid line) Pressure-Rate-of-Strain models.

flow configuration of the present DWP hydrocyclone is numerically simulated. The LPS model is used for the present simulations of several operative configurations, as it is widely recognized that QPS is less stable compared to the LPS. Outcomes of the LPS and QPS models are compared in Section 2.1 for the case with back-pressure 3035 Pa, already considered by Piller et al. (in press).

### 2.1. Model validation

The base mesh for the case BPS = 3035 Pa is selectively refined using the auto-adaption capability of ANSYS FLUENT™: all cells where the shear rate $\dot{\gamma}$ is in the upper quartile are refined. Two levels of refinement are tested and the simulations are advanced for two flow-through times on the refined meshes. The calculated results, not shown for brevity, are in satisfactory agreement between the base (finer) and the finest mesh, with a 3.5% (2.1%) maximum difference in the tangential velocity distribution within the barrel. Thus, the base mesh is deemed adequately refined for the purposes of the present investigation.

Modeling of the Pressure-Rate-of-Strain term affects the simulated swirling flow field within hydrocyclones, but it is still unclear to what extent (Brennan, 2006). The simulations of the considered hydrocyclone with BPS = 3035 Pa with either the LPS or the QPS models are compared in this section. Radial profiles of the axial, radial and tangential velocity components, of the static pressure and of the air volume fraction are compared at middle-height of the barrel. It is shown that the considered models yield analogous flow features.

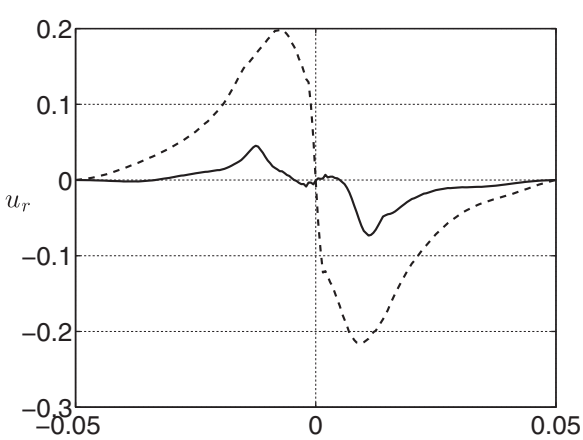


**Fig. 3.** Comparison of radial velocity $u_r$ in m/s for the case BPS = 3035 Pa, with either LPS (dashed line) or QPS (solid line) Pressure-Rate-of-Strain models.

The axial velocity is compared in Fig. 2. Results obtained with both models are in substantial agreement in the water phase, while LPS yields marginally lower velocity in the air core.

The radial velocity is compared in Fig. 3. The choice of the Pressure-Rate-of-Strain model has a strong impact on the magnitude of $u_r$, with the LPS and QPS yielding peak values as high as 0.2 m/s and 0.05 m/s, respectively. Nevertheless, the radial distribution of $u_r$ is similar between the two simulations, with peak locations placed at the air-core boundary.

The tangential velocity is compared in Fig. 4. $u_\theta$ is only marginally affected by the Pressure-Rate-of-Strain model, mostly within the air-core. This is encouraging, as in many respects $u_\theta$ is the most relevant quantity in hydrocyclones.

The air volume fraction is compared in Fig. 5. The LPS model yields a slightly more diffuse interface but the overall agreement between the two models is excellent.

## 3. Results

### 3.1. Overall flow pattern

Three-dimensional streamlines of the time-averaged velocity field for the case with BPS = 0 Pa allow to perceive the overall flow pattern. It is verified that streamlines originating from different locations on the same inlet port may show significantly dissimilar features. Thus, streamlines originating from at least two different points on any inlet surface are considered, aiming to provide a satisfactory representation of the flow field within the device. In Fig. 6a, a streamline originating

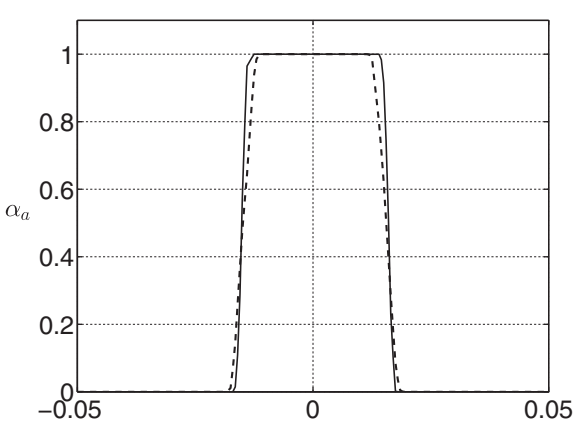


**Fig. 5.** Comparison of air volume fraction (dimensionless) for the case BPS = 3035 Pa, with either LPS (dashed line) or QPS (solid line) Pressure-Rate-of-Strain models.

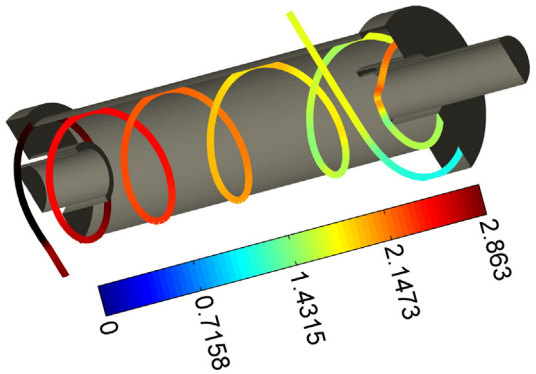


(a) Injection point on the MIP, leaving directly through the SIP.

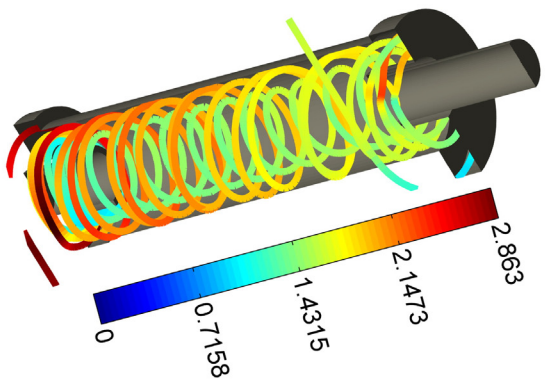


(b) Injection point on the MIP, leaving through the SIP after spiraling several times back and fort.

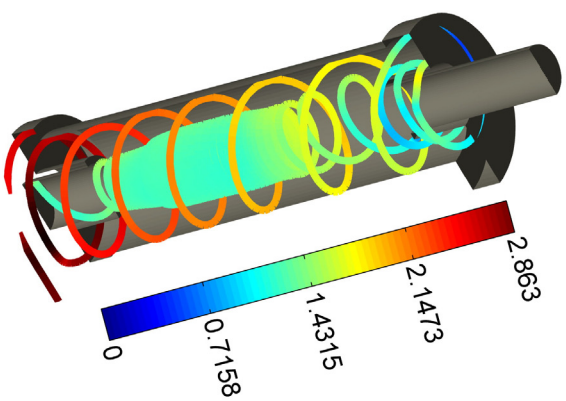


(c) Injection point on the MIP, leaving through the FLP.

**Fig. 6.** Streamlines colored by velocity magnitude, for BPS = 0 Pa and different injection points on inlet surfaces.

from the MIP spirals upwards reducing progressively its velocity, and eventually leaves the device through the SIP. In Fig. 6b, a streamline injected through the MIP spirals several times upwards and downwards throughout the barrel, eventually leaving the device through the SIP. In Fig. 6c, a streamline injected through the MIP eventually leaves the device through the FLP after hitting the top end-plate and overturning. The spiral's pitch for the descending flow is sensibly smaller than for the ascending flow due to the conservation of angular momentum and to a reduced water flow rate reported to the FLP. The air-streamlines shown in Fig. 6d and e originate from two distinct injection points on the FEP, located symmetrically with respect to the barrel's axis and leave the device through the FLP. Their markedly different patterns confirm the flow asymmetry within the device.

The following pattern can be thus conceived for DWP hydrocyclones within the considered range of BPS: a circulating fluid is injected through the MIP, spirals upwards forming a cylindrical layer close to

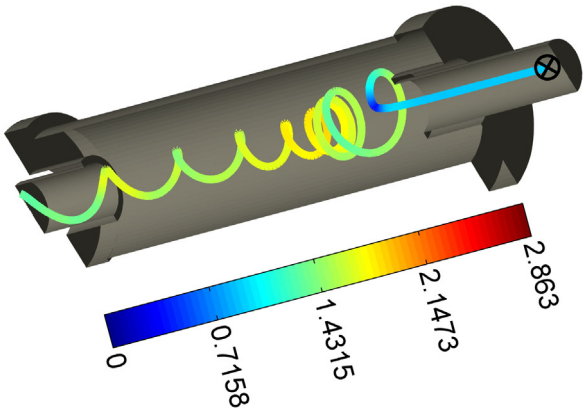


(d) Injection point on the feed port.

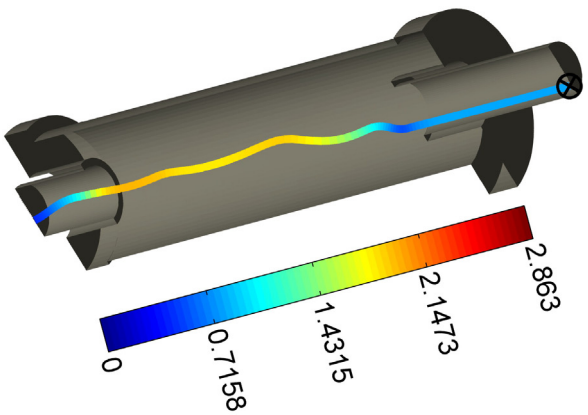


(e) Injection point on the feed port.

**Fig. 6** (*continued*).

the barrel's wall, hits against the top end-plate of the barrel and splits into two streams. One stream leaves the device through the SIP, the other flows back downwards towards the bottom barrel's end-plate forming an intermediate, coaxial layer. Part of the descending stream hits the bottom end-plate, overturns and joins the ascending stream. The remaining descending fluid leaves the device through the FLP. Atmospheric air enters the device through the FEP, forms a cylindrical core of air (AC hereafter) connecting the FEP to the FLP. The centrifugal acceleration forces the dense medium to the periphery of the barrel and constraints the lighter air phase within the AC, hindering the mixing between the two fluids.

### 3.2. Sensitivity to BPS

The operation of the considered hydrocyclone is sensibly affected by the imposed BPS. One of the most evident effects of progressively increasing the BPS is the monotonic decrease of the air volume contained within the device, as reported in Table 2. Centrifugal forces confine the air phase to the central part of the device: for all values of BPS, the air flows from the FEP to the FLP. For BPS ≥ 5000 Pa an air core is not formed within the device.

**Table 2**
Volume of air retained within the cyclone as per-cent of the barrel's volume.

| BPS [Pa] | $V_a/V_c$ [%] | BPS [Pa] | $V_a/V_c$ [%] |
|---|---|---|---|
| 0 | 26.80 | 3035 (QPS) | 16.40 |
| 1000 | 20.97 | 4000 | 14.07 |
| 2000 | 18.78 | 4500 | 12.17 |
| 3035 (LPS) | 16.62 | 5000 | 0 |

The *equivalent* AC diameter, $d_{AC}$, is conventionally defined as the region where the air volume fraction exceeds 0.5. The diameter of the locus of zero axial velocity (henceforth referred to as LZAV), $d_{LZAV}$, is conventionally defined as the *equivalent* (i.e., same volume) diameter of the region where the fluid flows downwards. The axial variation of $d_{AC}$ and $d_{LZAV}$ within the barrel for various BPS is shown in Fig. 7a. The variation of $d_{AC}$ and $d_{LZAV}$ with BPS is shown in Fig. 7b. The AC diameter (in red) decreases monotonically while moving from the FEP to the FLP, except in narrow regions close to the barrel's end-plates. The AC diameter decreases progressively with increasing BPS up to BPS = 4500 Pa, while it drops down abruptly to zero for BPS = 5000 Pa. The narrowing of the AC with increasing BPS is evident also in the profiles of the mean air volume fraction along several $x$-transects, at different axial locations along the barrel (Fig. 8). The time-averaged AC is nearly axis-symmetric for all values of BPS. As the BPS increases, the AC interface broadens, as is particularly evident for BPS = 4500 Pa (Fig. 8b). This feature has to be ascribed to an increasing instability of the AC, which *wobbles* about the centerline. As the time-averaged air volume fraction $\bar{\alpha}_a$ defines the amount of air per unit volume, regions where $0<\bar{\alpha}_a<1$ are occupied by the AC only occasionally.

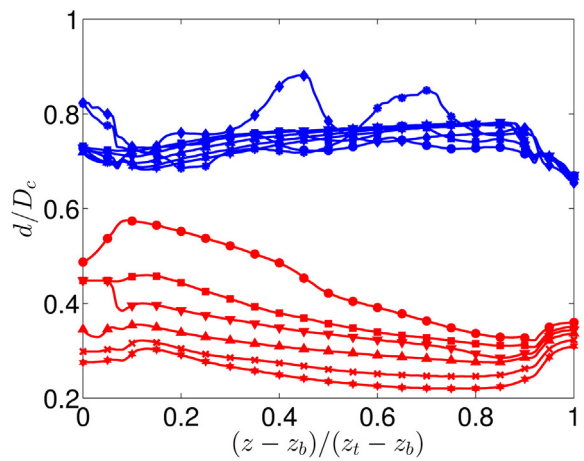


(a) Variation of $d_{AC}$ and $d_{LZAV}$, scaled with the barrel's diameter $D_c$, with the axial location or various BPS.

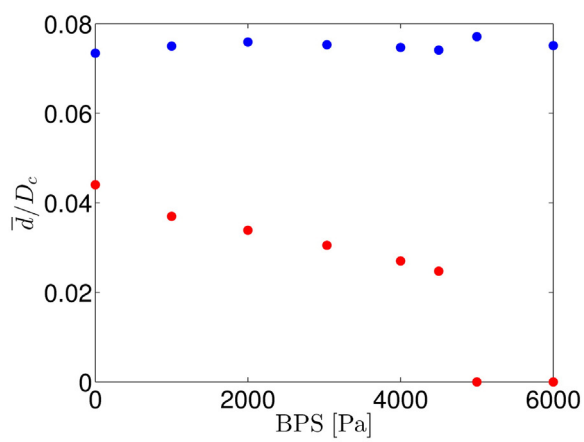


(b) Variation of the mean values of $d_{AC}$ and $d_{LZAV}$, scaled with the barrel's diameter $D_c$, with BPS.

**Fig. 7.** Variation of $d_{AC}$ (red) and $d_{LZAV}$ (blue) with respect to axial location and BPS. Symbols and corresponding BPS: ○ — 0 Pa, □ — 1000 Pa, ▽ — 2000 Pa, △ — 3035 Pa, × — 4000 Pa, ⋆ — 4500 Pa, ◇ — 5000 Pa, * — 6000 Pa. (For interpretation of the references to colour in this figure legend, the reader is referred to the web version of this article.)

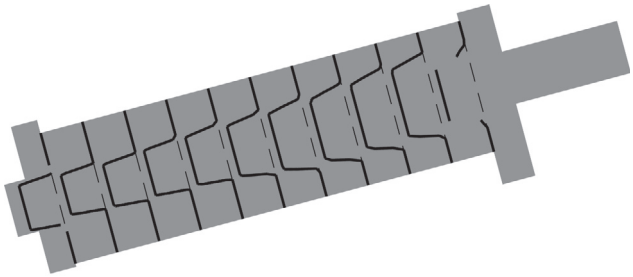

(a) BPS = 0 Pa, x− line.

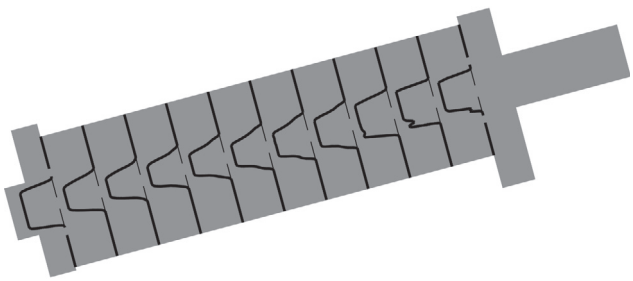

(b) BPS = 4500 Pa, x− line.

**Fig. 8.** Distribution of air volume fraction (dimensionless) for different values of BPS.

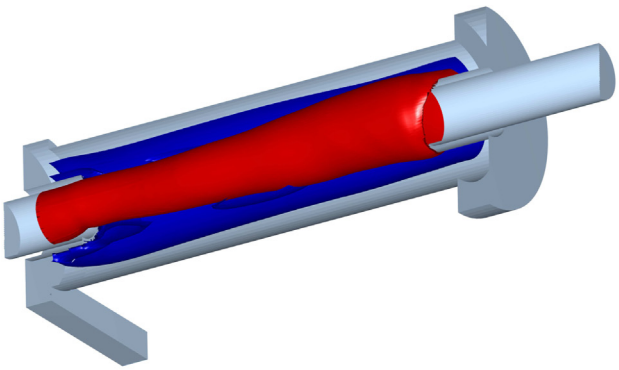

(a) BPS = 0Pa

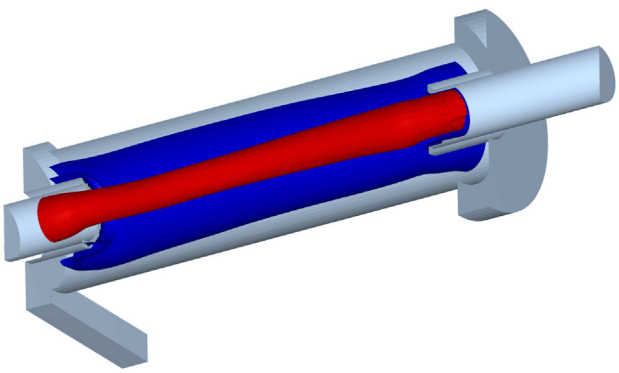

(b) BPS = 4500Pa

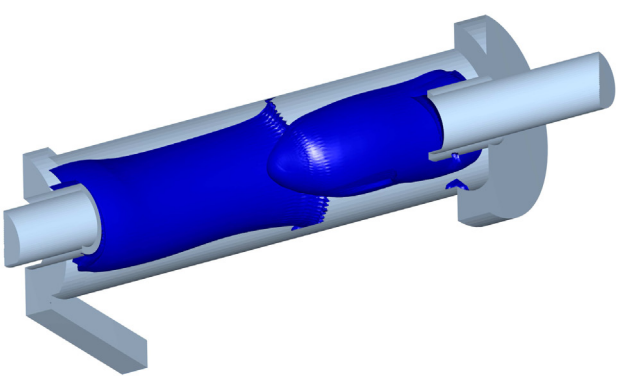

(c) BPS = 5000Pa

**Fig. 9.** Three-dimensional view of the air-core boundary (in red) and of the locus of zero axial velocity (in blue, sectioned with a $y-z$ plane), for different values of BPS. (For interpretation of the references to colour in this figure legend, the reader is referred to the web version of this article.)

Inspection of Fig. 7b suggests that the LZAV is nearly cylindrical and rather insensitive to BPS: indeed, as is shown in a later Section 3.4.1, the axial velocity profile within the ascending flow region is nearly unaffected by BPS.

As already mentioned, for BPS≥5000 Pa the flow pattern is entirely different, with two apparently separated circulation regions located in the top and bottom parts of the barrel. Fig. 9 shows the three-dimensional view of the AC and LZAV for BPS in the range 0÷5000 Pa: for BPS≥5000 Pa the LZAV is split into two distinct recirculation regions, as evident in Fig. 9c. Nevertheless, the water flow-split reported in Table 3 suggests that water is exchanged between the two recirculation regions, with a net flow of water from the uppermost to the lowermost region. Visual analysis of the streamline patterns shown in Fig. 10 for the case BPS = 6000 Pa suggests that water entering through the sink port is conveyed partly to the feed port (Fig. 10a), partly to the float port, entering the lower recirculation bubble (Fig. 10b). The entire flow stream of water injected through the medium inlet port is conveyed to the float port (Fig. 10c).

The volume flow-rate distributions of water and air for different values of BPS are reported in Table 3 as per-cent fractions of the water volume flow-rate injected through the MIP. On the third column, $V_{\cdot w,\mathrm{sink}}$ is akin to the underflow-to-throughput ratio used to characterize cylindrical-conical hydrocyclones. This quantity decreases with increasing BPS, except for a peak at BPS = 4000 Pa. The flow rates through all openings experience an abrupt change for 4500<BPS<5000 Pa.

The dependence of the total pressure at the MIP on the BPS is shown in Fig. 11. As expected, the larger the BPS the larger the pressure required to maintain a constant volume flow rate through the MIP. Not as intuitive is the linear dependence evident in Fig. 11, in particular when considering the augmented flow rate through the FLP. The corresponding Euler number, defined as

$$\mathrm{Eu} \equiv \frac{\Delta p}{\rho w V_c^2/2};\quad \Delta p \equiv (p_{in} - \mathrm{BPS});\quad V_c \equiv \frac{4Q}{\pi D_c^2} \tag{1}$$

decreases monotonically with increasing BPS, as shown in Table 4. According to Silva et al. (2015), in traditional cyclones this suggests that a constant throughput can be maintained with progressively lower energy consumption.

The *instability* $S_w$ of the water flow through the FLP and SIP, conventionally defined here as the ratio of the standard deviation to the mean value of the volume flow-rate through each port, increases with increasing BPS up to BPS = 4500 Pa, while it decreases abruptly when further increasing BPS (see Table 5). The only noticeable exception to this trend is the relatively high instability of water flow through the FLP at BPS = 0 Pa.

**Table 3**
Water and air volume flow-rate distributions for different values of BPS, as per-cent fractions of the water volume flow-rate injected through the MIP. Positive values denote flow *into* the device, negative values denote flow *leaving* the device. (LPS) and (QPS) identify simulations using either the LPS or the QPS Pressure-Rate-of-Strain model, respectively.

| BPS [Pa] | $V_{\cdot w,\mathrm{float}}$ [%] | $V_{\cdot w,\mathrm{sink}}$ [%] | $V_{\cdot w,\mathrm{feed}}$ [%] | $V_{\cdot a,\mathrm{float}}$ [%] | $V_{\cdot a,\mathrm{feed}}$ [%] |
|---|---|---|---|---|---|
| 0 | −14.40 | −85.61 | 0 | −81.02 | 81.02 |
| 1000 | −22.58 | −77.41 | 0 | −102.39 | 102.39 |
| 2000 | −29.70 | −70.51 | 0 | −88.61 | 88.61 |
| 3035 (LPS) | −39.32 | −60.69 | 0 | −68.36 | 68.36 |
| 3035 (QPS) | −39.03 | −60.87 | 0 | −80.81 | 80.81 |
| 4000 | −52.90 | −47.10 | 0 | −47.46 | 47.46 |
| 4500 | −63.67 | −36.17 | 0 | −45.98 | 45.98 |
| 5000 | −163.44 | 93.018 | −29.58 | 0 | 0 |
| 6000 | −175.3 | 110.70 | −35.40 | 0 | 0 |

Based on the aforementioned results, a parallelism might be conceived between the cylindrical-conical and the DWP hydrocyclones. Increasing the BPS is akin to reducing the spigot area and yields similar consequences: the fluid recovery to the sink (underflow) decreases, the air core shrinks progressively and eventually disappears, the Euler number decreases.

### 3.3. Effects of dense medium properties

In actual applications of centrifugal dense medium separators (DMS hereafter) the dense medium is made up with fine-ground magnetite (specific density 4.85) or atomized ferrosilica (specific density 6.7 ÷ 7.1 at a concentration of 15% Si by weight) depending on the required cut density. The raw material undergoing separation is pre-treated on a screen to remove fine material (e.g. minus 500 micron) that can contaminate the dense medium powders. Even so, during operation the medium becomes contaminated by the fines of non-magnetic materials entering with the raw feed due to pre-screening inefficiency or produced by handling and abrasion of the material being treated. The separation medium exits the device with the separation products sink and float and is drained on a horizontal screen and directly recirculated to the separator. The fraction of medium that escapes the first drainage is washed out causing the dilution of the medium. The diluted medium is treated and the contamination is mitigated and contained by the magnetic separators in the medium regeneration section of the DMS plant.

Experimental measurements (Lapasin et al., 1988; Lapasin and Schena, 1990) show that the dynamic viscosity of a contaminated dense medium depends mainly on the volume concentration of the solid phase. This, in turn, implies that once the type and density of the suspension (i.e., either water/magnetite or water/ferrosilica) and the degree of contamination are determined, the dynamic viscosity of the dense medium is uniquely determined. A model capable of predicting the viscosity of contaminated magnetite suspensions as a function of the solid composition and of the shear rate expected within a DMS is proposed by Lapasin et al. (1988) and Lapasin and Schena (1990). The combined effect of changing density and viscosity of the dense medium is investigated here by considering a single-phase fluid with the same density and viscosity of a contaminated water/magnetite suspension of assigned *total disperse phase volume fraction* $\phi = 20\%$ and *contaminant volume fraction in the disperse phase* $\chi = 30\%$. The relative densities of the magnetite and the contaminant are assumed $\rho_m = 4.85$ and $\rho_c = 1.63$, respectively, yielding a relative medium density $\rho_{dm} = 1.58$:

$$\begin{aligned} \rho_{ss} &= \rho_m(1-\chi) + \rho_c\chi \quad \text{(density of solid suspension)} \\ \rho_{dm} &= \rho_{ss}\phi + (1-\phi) \qquad \text{(density of dense medium)} \end{aligned} \tag{2}$$

According to Lapasin et al. (1988) and Lapasin and Schena (1990), water/magnetite suspensions behave as pseudoplastic fluids, whose relative viscosity depends on the shear rate $\dot{\gamma}$:

$$\dot{\gamma} \equiv \sqrt{2\sum_{i,j} D_{ij}D_{ij}} \tag{3}$$

where $D_{i\,j}$ denotes the strain-rate tensor. A power-law fit to the rheological model proposed by Lapasin et al. (1988) and Lapasin and Schena (1990) is used to define the relative viscosity–shear rate dependence for the considered dense medium (see Fig. 12).

A simulation with the dense medium and 3035 Pa BPS is carried out, yielding the following characteristic quantities:

- underflow-to-throughput ratio: 69.8%,
- Euler number: 744,
- per-cent volume of the barrel occupied by the air core: 18.6%,
- mean LZAV diameter (scaled by $D_c$): 0.74,
- mean air core diameter (scaled by $D_c$): 0.33,
- maximum, minimum and volume-averaged relative dynamic viscosity: 3.28, 2.47, 3.13.

Comparing the results at BPS = 3035 Pa for the Newtonian (Table 4) and non-Newtonian fluids, the following remarks can be drawn:

1. The Euler number is larger for the non-Newtonian fluid, denoting a lower hydraulic efficiency of the device, coherent with the overall rise of viscosity.
2. The underflow-to-throughput ratio is larger when the DWP is operated with the non-Newtonian fluid, while the volume of the air core increases.

The axial, radial and tangential velocity profiles at the barrel's midplane are shown in Fig. 13. Data obtained by injecting water or the considered, non-Newtonian fluid are compared. Minor differences are experienced by the tangential and axial velocity components while the radial velocity is sensibly reduced with the non-Newtonian fluid.

### 3.4. Velocity field

In the following, a thorough description of the flow field throughout the device is provided only for the two limiting cases BPS = 0 Pa and BPS = 4500 Pa. Results from the whole set of simulations are compared only on the *x*-axis passing through the barrel's transverse mid-plane, henceforth referred to as *x-transect*.

#### 3.4.1. Axial velocity

Profiles of axial velocity on the *x*-transect are reported in Fig. 14. The maximum velocity within the air core increases with increasing BPS up to BPS = 1000 Pa, little change is observed for $1000 \le \mathrm{BPS} \le 2000$ Pa while it decreases significantly beyond this range of BPS. For all considered values of BPS, the air core flows axially much faster than the surrounding water, confirming findings by Piller et al. (in press).

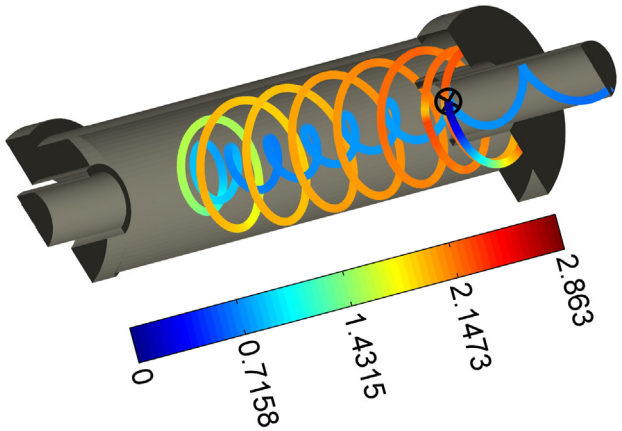


(a) Injection point on SIP, leaving through the FEP.

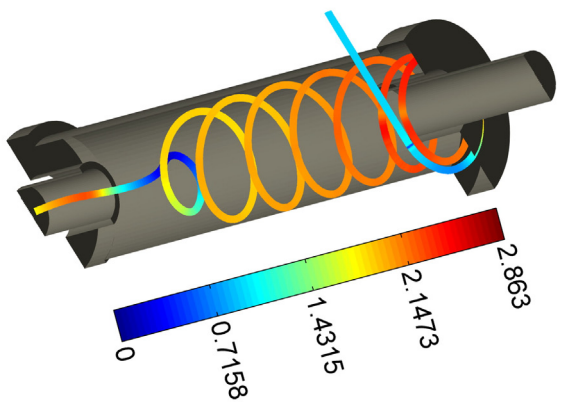


(b) Injection point on SIP, leaving through the FLP.

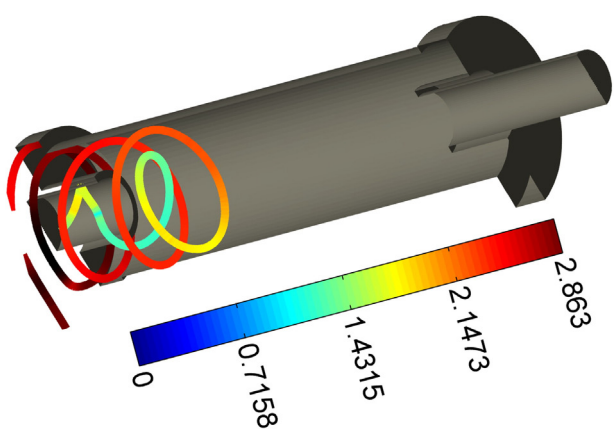


(c) Injection point on MIP, leaving through the FLP.

**Fig. 10.** Streamlines colored by velocity magnitude, for BPS = 6000 Pa and different injection points, marked by a symbol.

Fig. 15 provides an overview of the axial velocity distribution throughout the device. The blue marks identify locations of zero axial velocity: three close blue marks denote flow recirculation. Recirculation regions, located close and below the air core, can be identified for BPS = 0 Pa (Figs. 9a, 15a) and BPS = 1000 Pa (not shown for brevity). With increasing BPS the axial velocity distribution within the descending water layer becomes more uniform. The recirculation bubbles disappear for higher values of BPS. For BPS ≥ 5000 Pa the flow separates into an upper and a lower recirculation regions, whose axial separation plane is displaced towards the FLP as BPS increases.

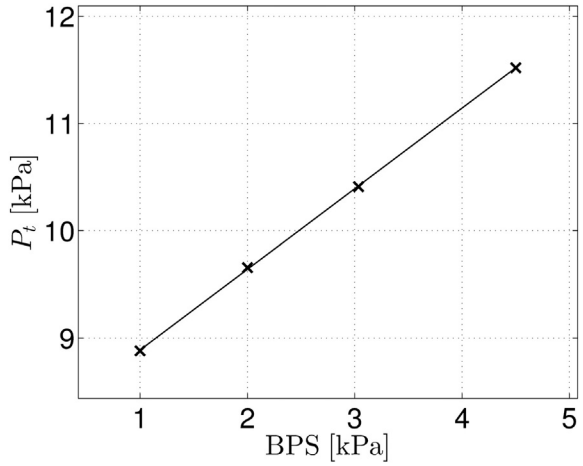


**Fig. 11.** Dependence of the total pressure at the MIP on the BPS. Symbols: numerical results. The solid line represents a linear regression.

*3.4.2. Radial velocity*

Fig. 16 compares profiles of radial velocity, for all considered values of BPS, on the *x*-transect passing through the center of the barrel. The radial velocity component is about one order of magnitude smaller than the axial velocity. In normal operation mode, the radial velocity peaks at or near the AC interface. The radial velocity component is negligibly small in water for BPS = 0 Pa, then increases for BPS ≤ 2000 Pa and does not decrease significantly beyond this value of BPS. Much higher values of $u_r$ are found within the AC. The most striking feature of Fig. 16 is the sign change in $u_r$ throughout the axis, implying that the fluid flows towards negative *x* throughout the *x*-transect.

Two isosurfaces corresponding to opposite values of $u_r$, are reported in Fig. 17 for both BPS = 0 Pa and BPS = 4500 Pa. A definite helicoidal structure is evident for both values of BPS.

An overview of the distribution of $u_r$ throughout the device for both BPS = 0 Pa and BPS = 4500 Pa is provided in Fig. 18. It is noticed that $u_r$ depends significantly on *z*, e.g., for BPS = 4500 Pa $u_r$ has different orientations in the top and bottom halves of the barrel, as expected due to the helicoidal pattern represented in Fig. 17.

*3.4.3. Tangential velocity*

Profiles of tangential velocity along the x-transect on the barrel's midplane are reported in Fig. 19 for all considered values of BPS. The tangential velocity component within the ascending water layer is rather insensitive to changes in BPS, suggesting that the ascending flow pattern is mainly dictated by the imposed flow rate at the MIP. The tangential velocity within the descending water layer increases monotonically while increasing BPS up to 4500 Pa. Clearly, the tangential

**Table 4**
Dependence of the Euler number on the BPS.

| BPS [Pa] | 0 | 1000 | 2000 | 3035 | 4500 |
|---|---|---|---|---|---|
| Eu | 776 | 744 | 723 | 697 | 663 |

**Table 5**
Instability of water flow through the SIP and FLP, for different values of BPS.

| BPS [Pa] | $S_w$ [%], sink | $S_w$ [%], float |
|---|---|---|
| 0 | 0.13 | 1.43 |
| 1000 | 0.13 | 0.52 |
| 2000 | 0.24 | 0.78 |
| 3035 (LPS) | 0.42 | 1.85 |
| 3035 (QPS) | 0.51 | 1.19 |
| 4000 | 2.11 | 4.37 |
| 4500 | 4.64 | 5.93 |
| 5000 | 0.21 | 0.13 |
| 6000 | 0.52 | 0.82 |

velocity profile does not conform to a Rankine vortex model, being roughly radially uniform for BPS≥2000 Pa within the descending water layer. An overview of the distribution of $u_\vartheta$ throughout the device for both BPS = 0 Pa and BPS = 4500 Pa is provided in Fig. 20. For BPS = 0 Pa the tangential velocity in the water layer decreases axially from the MIP towards the SIP and increases radially towards the wall. For BPS = 4500 Pa, $u_\vartheta$ in the water layer does not change significantly along the axial direction and increases weakly towards the barrel's wall. $u_\vartheta$ is very low within the AC, though increasing as the AC is rotationally accelerated towards the FLP. It is verified that for BPS≥5000 Pa the swirl direction is inverted close to the top of the barrel as water is injected through the sink port.

The centrifugal force per unit mass is shown in Fig. 21: it peaks at the AC interface and decreases as ~1/$r$ with increasing radius within the descending water layer. For BPS≤2000 Pa a second peak is evident at the LZAV.

### 3.4.4. Static pressure

Profiles of static pressure are compared in Fig. 22, on the $x$-transect passing through the center of the barrel, for all considered values of BPS. The static pressure increases monotonically with increasing BPS throughout the transect: this is due to the combined increase of BPS and the total pressure at the MIP and to the increase of the centrifugal force.

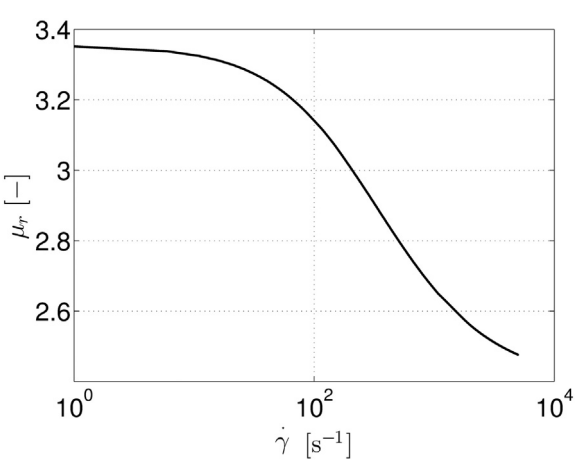


**Fig. 12.** Relative viscosity–shear rate dependence for a contaminated water/magnetite suspension of assigned solid concentration $\phi = 20\%$ and contaminant concentration $\chi = 30\%$ by volume, according to the model by Lapasin et al. (1988) and Lapasin and Schena (1990).

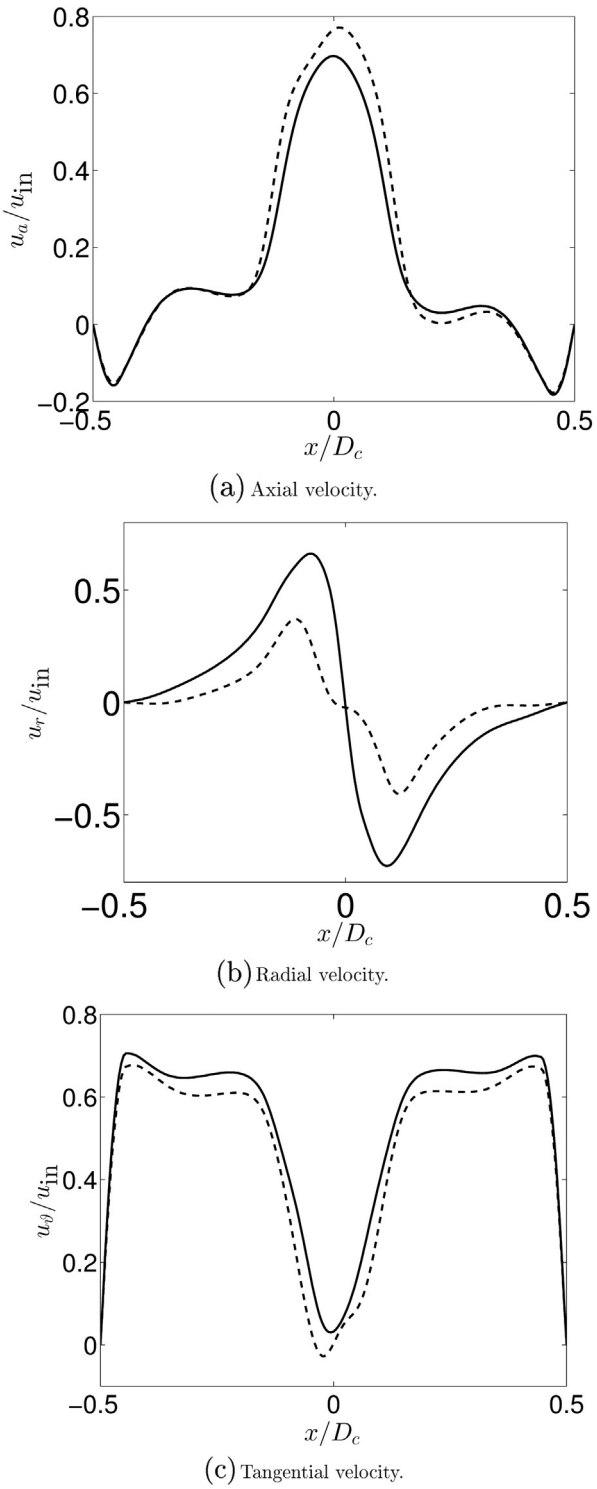


**Fig. 13.** Profiles of (a) axial, (b) radial and (c) tangential velocity at the barrel's midplane for the case 3035 Pa BPS with either Newtonian (plain water) or non-Newtonian (water/magnetite) dense medium. The radial velocity component is magnified by a factor of 10. Dashed lines refer to the non-newtonian fluid, solid lines to the newtonian fluid.

## 4. Turbulence

The distribution of the turbulent viscosity ratio $\mu_r \equiv \mu_t/\mu$ on a $x-z$ plane is shown in Fig. 23 for BPS = 0 Pa and 4500 Pa. $\mu_r$ increases with increasing BPS and is sensibly larger in the uppermost region of the

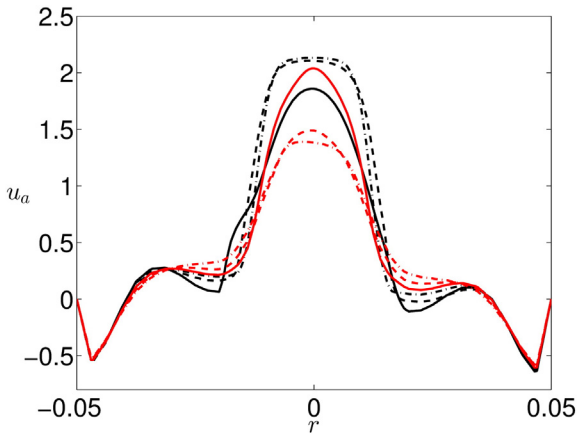


**Fig. 14.** Profiles of axial velocity $u_a$ in m/s, for all considered values of BPS, on the $x$-transect passing through the center of the barrel. Black lines: BPS = 0 Pa (solid), BPS = 1000 Pa (dashed), BPS = 2000 Pa (dash-dot). Red lines: BPS = 3035 Pa (solid), BPS = 4000 Pa (dashed), BPS = 4500 Pa (dash-dot). (For interpretation of the references to colour in this figure legend, the reader is referred to the web version of this article.)

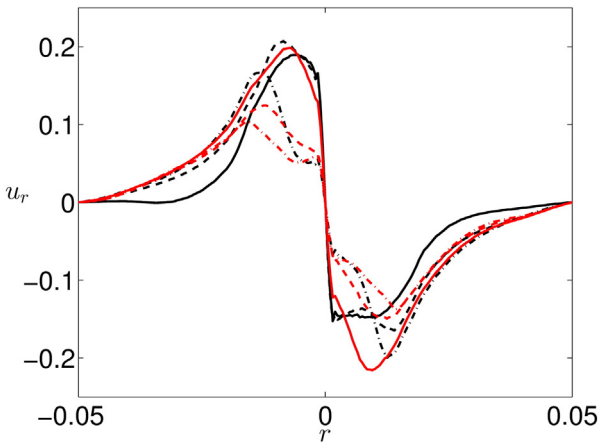


**Fig. 16.** Profiles of radial velocity $u_r$ in m/s, for all considered values of BPS, on the $x$-transect passing through the center of the barrel. Black lines: BPS = 0 Pa (solid), BPS = 1000 Pa (dashed), BPS = 2000 Pa (dash-dot). Red lines: BPS = 3035 Pa (solid), BPS = 4000 Pa (dashed), BPS = 4500 Pa (dash-dot). (For interpretation of the references to colour in this figure legend, the reader is referred to the web version of this article.)

barrel, where the ascending fluid hits the upper end-plate and overturns. With increasing BPS, a larger amount of fluid is recirculated towards the FLP causing the region of large $\mu_r$ to extend downwards. The AC region is nearly laminar.

## 5. Concluding remarks

DWP cyclones have been widely and successfully used in processing plants but not as extensively studied as the classical *cone in cylinder ones*. The two silhouettes determine quite different flow patterns. The two-phase hydro-dynamics of a DWP (cylindrical) hydro-cyclone is explored by numerical simulation.

Three-dimensional visualizations with velocity-colored fluid stream-lines and isosurfaces of the water/air interface and of the LZAV mantle are used to easy the understanding of the complex flow pattern

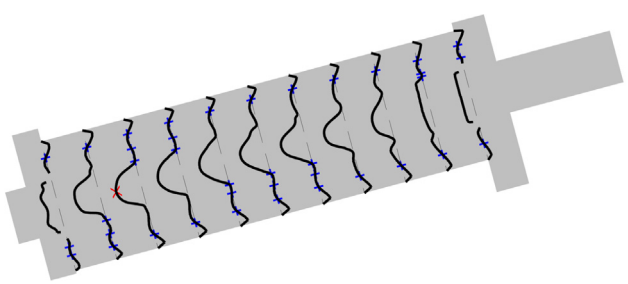

(a) BPS = 0Pa, $x-$line. Red mark denotes location of maximum absolute velocity 1.94 m/s.

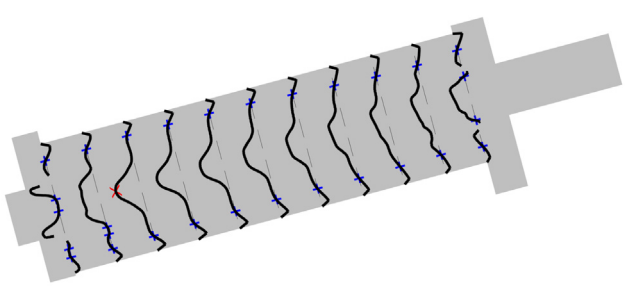

(b) BPS = 4500Pa, $x-$line. Red mark denotes location of maximum absolute velocity 1.78 m/s.

**Fig. 15.** Distribution of axial velocity $u_a$ in m/s for different values of BPS. Blue marks denote locations of zero velocity. (For interpretation of the references to colour in this figure legend, the reader is referred to the web version of this article.)

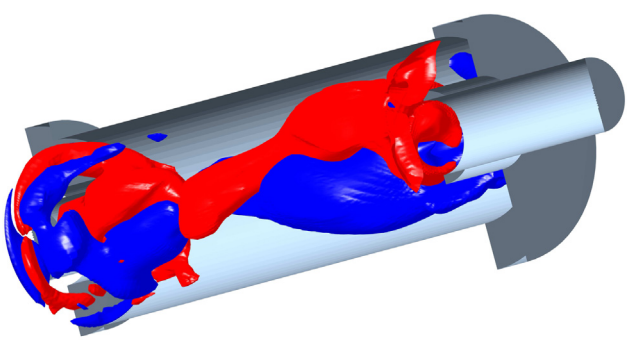

(a) BPS = 0 Pa.

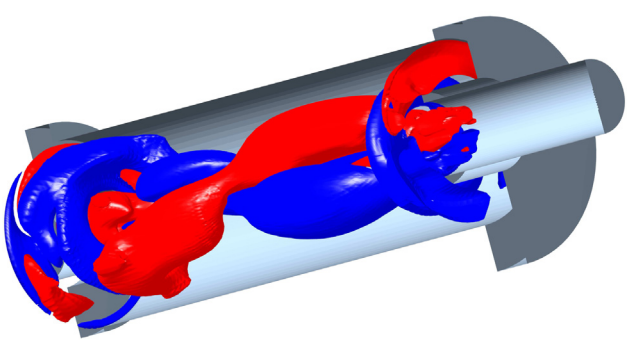

(b) BPS = 4500 Pa.

**Fig. 17.** Isosurfaces of positive (red) and negative radial velocity for BPS = 0 Pa and BPS = 4500 Pa. (For interpretation of the references to colour in this figure legend, the reader is referred to the web version of this article.)

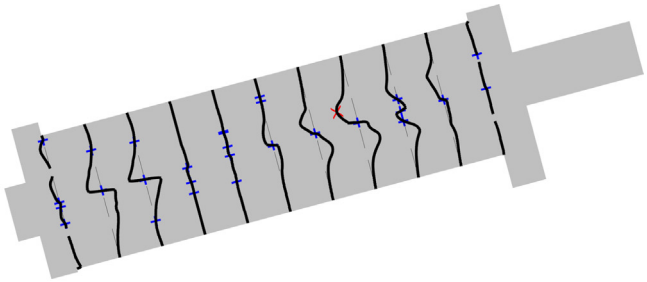

(a) BPS = 0 Pa, $x-$line. Red mark denotes location of maximum absolute velocity 0.49 m/s.

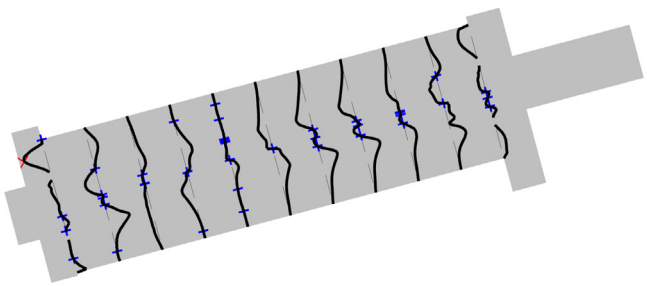

(b) BPS = 4500 Pa, $x-$line. Red mark denotes location of maximum absolute velocity 0.26 m/s.

**Fig. 18.** Distribution of radial velocity $u_r$ in m/s for different values of BPS. Blue marks denote locations of zero velocity. (For interpretation of the references to colour in this figure legend, the reader is referred to the web version of this article.)

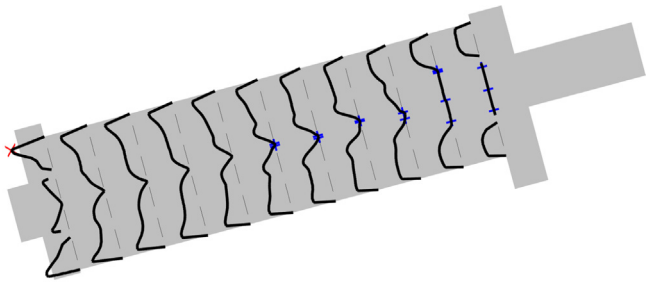

(a) BPS = 0Pa, $x-$line. Red mark denotes location of maximum absolute velocity 3.02 m/s.

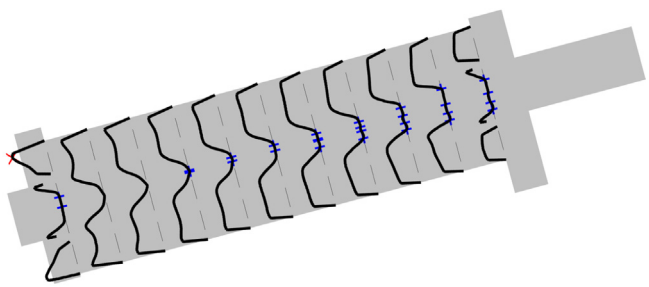

(b) BPS = 4500Pa, $x-$line. Red mark denotes location of maximum absolute velocity 3.13 m/s.

**Fig. 20.** Distribution of tangential velocity $u_\theta$ in m/s for different values of BPS. Blue marks denote locations of zero velocity. (For interpretation of the references to colour in this figure legend, the reader is referred to the web version of this article.)

in the interior of the DWP. The effect of changing the back-pressure at the tangential discharge orifice is investigated in this study. With respect to the traditional design, the examined reverse-flow cylindrical hydro-cyclone has a different shape of the tangential velocity profile that is roughly radially uniform outside the air core, except close to the barrel's wall. This distinct behavior reflects in the centrifugal acceleration profile and characterizes the entire, investigated range of back-pressure.

Starting from a condition of zero back-pressure as the counter-pressure is increased the air core shrinks and snakes up to almost disappear. In contrast and unexpectedly the isosurface of zero axial velocity is

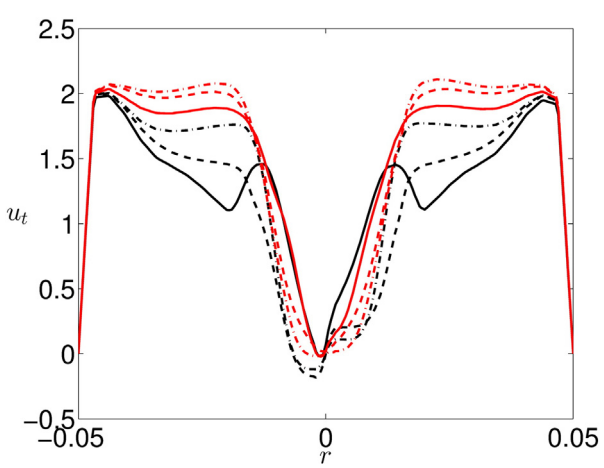


**Fig. 19.** Profiles of tangential velocity $u_\theta$ in m/s, for all considered values of BPS, on the $x$-transect passing through the center of the barrel. Black lines: BPS = 0 Pa (solid), BPS = 1000 Pa (dashed), BPS = 2000 Pa (dash-dot). Red lines: BPS = 3035 Pa (solid), BPS = 4000 Pa (dashed), BPS = 4500 Pa (dash-dot). (For interpretation of the references to colour in this figure legend, the reader is referred to the web version of this article.)

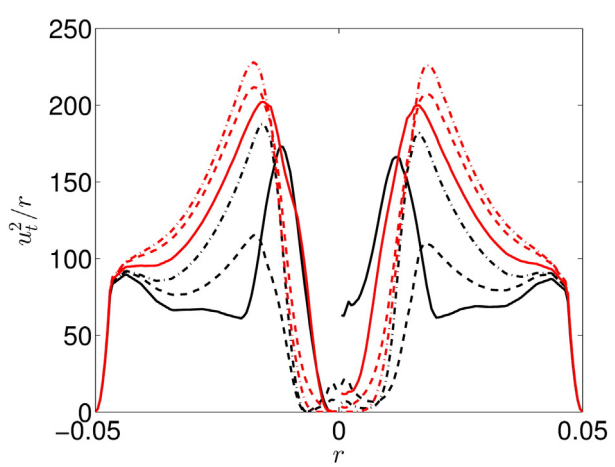


**Fig. 21.** Profiles of mass-specific centrifugal force $u_t^2/r$ in $m/s^2$ , for all considered values of BPS, on the $x$-transect passing through the center of the barrel. Black lines: BPS = 0 Pa (solid), BPS = 1000 Pa (dashed), BPS = 2000 Pa (dash-dot). Red lines: BPS = 3035 Pa (solid), BPS = 4000 Pa (dashed), BPS = 4500 Pa (dash-dot). (For interpretation of the references to colour in this figure legend, the reader is referred to the web version of this article.)

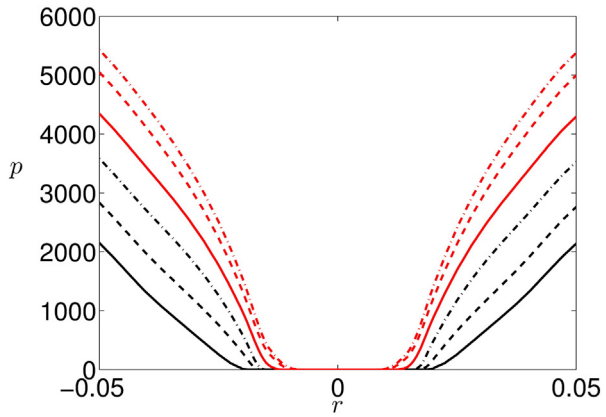


**Fig. 22.** Profiles of static pressure, for all considered values of BPS, on the $x$-transect passing through the center of the barrel. Black lines: BPS = 0 Pa (solid), BPS = 1000 Pa (dashed), BPS = 2000 Pa (dash-dot). Red lines: BPS = 3035 Pa (solid), BPS = 4000 Pa (dashed), BPS = 4500 Pa (dash-dot). (For interpretation of the references to colour in this figure legend, the reader is referred to the web version of this article.)

steady and maintains its shape and diameter in a relatively wide range of back-pressure. By increasing the back-pressure less fluid is reported to the upper tangential discharge orifice. Surprisingly the magnitude of the upward axial velocity does not fall greatly instead more ascending fluid is reversed at the top of the cyclone and directed downward. At zero or low BPS (i.e., <1500 Pa) two small fluid recirculation bubbles are present closed to the air core. These come together, coalesce and finally disappear at much higher back-pressure. As the back-pressure overtakes a certain threshold (namely 4500–5000 Pa in the scrutinized case study) the already thin air core completely vanishes and the hydrodynamics of the device changes suddenly. Two recirculation regions appear: one at the top and the other at bottom of the cylinder. These regions are both fed by fluid; the top region by the fluid re-entering from the tangential orifice due to excess of back-pressure, the bottom region is fed by the entering media. It is verified that the two regions exchange fluid.

An *optimum* range of back-pressure exists (i.e., 1500 ÷ 4500 Pa for the considered device) for normal operational behavior. For preventing abnormal local fluid recirculation phenomena the back-pressure should be above the lower threshold limit of the *optimum* range. The appearance of two large recirculating regions for operating back-pressure pressures above the upper BPS range boundary alters the normal functioning of the device.

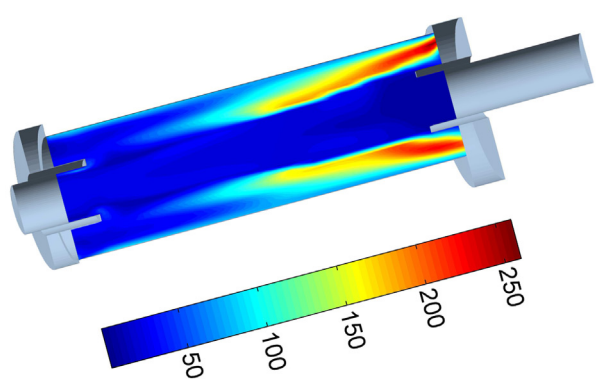


(a) BPS = 0 Pa, $x-$line.

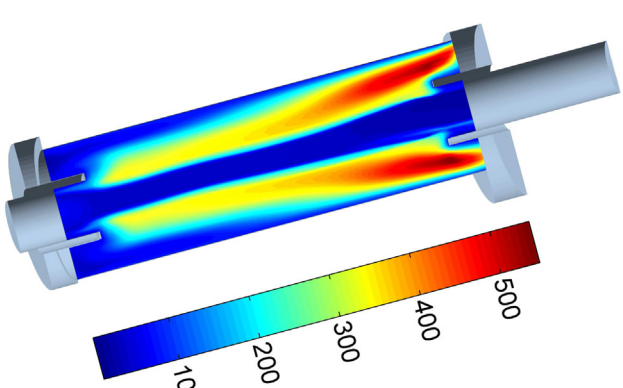


(b) BPS = 4500 Pa, $x-$line.

**Fig. 23.** Distribution of viscosity ratio (dimensionless) for different values of BPS.

## Acknowledgments

The authors gratefully acknowledge the financial support of the University of Trieste via the PILLER_FRA_2014 project.

## References

Baillie, D., Shah, C., Heiey, A., 1997. Three-product larcodems separator demonstration, installation and performance testing. Technical Coal Research Series, European Commission, Office for Official Publications of the European Communities, Brussels, Luxembourg, 1997 (ISBN 92–827–9273-0).

Belardi, G., Bozano, P., Mencinger, J., Piller, M., Schena, G., 2014. Numerical simulation of water–air flow pattern in a tri-flo®cylindrical separator. Proceedings of the XXVII International Mineral Processing Congress, Santigo , Chile.

Brennan, M., 2006. Cfd simulations of hydrocyclones with an air core: comparison between large eddy simulations and a second moment closure. Chem. Eng. Res. Des. 84 (6 A), 495–505. http://dx.doi.org/10.1205/cherd.05111 (cited By 46).

Brennan, M.S., Holtham, P.N., Rong, R., Lyman, G.J., 2002. Computational fluid dynamic simulation of dense medium cyclones. *Proceedings 9th Australian coal Preparation conference*, Yeppoon, Australia (October, Paper B3).

Chiné, B., Concha, F., 2000. Flow patterns in conical and cylindrical hydrocyclones. Chem. Eng. J. 80 (1–3), 267–273. http://dx.doi.org/10.1016/S1383–5866(00)00101–5 (cited By 40).

Chiné, B., Ferrara, G., 1997. Comparison between flow velocity profiles in conical and cylindrical hydrocyclones. Kona Powder Part. J. 15 (May), 170–179. http://dx.doi.org/10.14356/kona.1997021 (cited By 3).

Cullivan, J.C., Williams, R.A., Cross, C.R., 2003. Understanding the hydrocyclone separator through computational fluid dynamics. Chem. Eng. Res. Des. 81 (4), 455–466. http://dx.doi.org/10.1205/026387603765173718 (cited By 68).

Ferrara, G., 1995. State-of-the-art and new developments in dense medium separation processes. Mineral Processing: Recent Advances and Future Trends : Proceedings of a Conference Honouring Professor P. C. Kapur on His 60th Birthday. Indian Institute of Technology, Kanpur (December 11–15).

Ferrara, G., Ruff, H.J., 1982. Dynamic dense medium separation processes — 1. Erzmetall: J. Explor. Min. Metall. 35 (6), 294–299 (cited By 4).

Hsieh, K.T., Rajamani, R.K., 1991. Mathematical model of the hydrocyclone based on physics of fluid flow. AIChE J 37 (5), 735–746 (cited By 151).

Lapasin, R., Schena, G.D., 1990. Modelling the rheological behaviour of dense media for coal processing. Coal Prep. 8 (3–4), 167–183. http://dx.doi.org/10.1080/07349349008905183 (cited By 2).

Lapasin, R., Ferrara, G., Ruscio, E., Schena, G.D., 1988. Rheological characterization of magnetite dense media. Coal Prep. 5 (3–4), 167–183. http://dx.doi.org/10.1080/07349348808945564 (cited By 5).

Launder, B.E., 1989. Second-moment closure: present … and future? Int. J. Heat Fluid Flow 10 (4), 282–300. http://dx.doi.org/10.1016/0142-727X(89)90017–9 (cited By 360).

Launder, B.E., Reece, G.J., Rodi, W., 1975. Progress in the development of a Reynolds-stress turbulence closure. J. Fluid Mech. 68, 537–566.

Lilly, D.K., 1966. On the application of the eddy viscosity concept in the inertial subrange of turbulence. NCAR Manuscript 123. National Center for Atmospheric Research.

Miller, J.D., Van Camp, M.C., 1982. Fine coal flotation in a centrifugal field with an air sparged hydrocyclone. Min. Eng. 34 (11), 1575–1580 (cited By 14).

Piller, M., Mencinger, J., Schena, G., Belardi, G., 2016. Two-phase flow field in a cylindrical hydrocyclone with tangential discharge. Int. J. Fluid Mech. Res. (In press).

Pope, S.B., 2000. Turbulent Flows. Cambridge University Press (ISBN 9780521598866).

V. Rakowsky. Centrifugal method and apparatus for separating solids, December 15, 1959. URL http://www.google.com/patents/US2917173 . US Patent 2,917,173.

H. Ruff. Dynamic dense media separator, 1980. United States Patent 4216095.

Silva, D.O., Vieira, L.G.M., Barrozo, M.A.S., 2015. Optimization of design and performance of solid–liquid separators: a thickener hydrocyclone. Chem. Eng. Technol. 38 (2), 319–326. http://dx.doi.org/10.1002/ceat.201300464 (cited By 5).

Slack, M.D., Wraith, A.E., 1997. Modelling the velocity distribution in a hydrocyclone. *4th International Colloquium on Process Simulation*, Pages 65–83, Espoo, Finland (June).

Slack, M.D., Prasad, R.O., Bakker, A., Boysan, F., 2000. Advances in cyclone modelling using unstructured grids. Chem. Eng. Res. Des. 78 (8), 1098–1104. http://dx.doi.org/10.1205/026387600528373 (cited By 141).

Smagorinsky, J., 1963. General circulation experiments with the primitive equation. I. The basic experiment. Mon. Weather Rev. 91, 99–164.

Speziale, C.G., Sarkar, S., Gatski, T.B., 1991. Modelling the pressure–strain correlation of turbulence: an invariant dynamical systems approach. J. Fluid Mech. 227, 245–272. http://dx.doi.org/10.1017/S0022112091000101 (cited By 849).

Suasnabar, D.J., 2000. Dense Medium Cyclone Performance, Enhancements Via Computational Modeling of the Physical Process PhD Thesis University of New South Wales.

Wills, B.A., 1988. Mineral processing technology. International Series on Materials Science & Technology, fourth ed. Pergamon Press.